

# Atomic-Scale Visualization of Quantum Interference on a Weyl Semimetal Surface by Scanning Tunneling Microscopy

Hao Zheng,<sup>†,■</sup> Su-Yang Xu,<sup>†,■</sup> Guang Bian,<sup>†,■</sup> Cheng Guo,<sup>‡</sup> Guoqing Chang,<sup>§,||</sup> Daniel S. Sanchez,<sup>†</sup> Ilya Belopolski,<sup>†</sup> Chi-Cheng Lee,<sup>§,||</sup> Shin-Ming Huang,<sup>§,||</sup> Xiao Zhang,<sup>‡</sup> Raman Sankar,<sup>⊥</sup> Nasser Alidoust,<sup>†</sup> Tay-Rong Chang,<sup>#,†</sup> Fan Wu,<sup>▽</sup> Titus Neupert,<sup>●</sup> Fangcheng Chou,<sup>⊥</sup> Horng-Tay Jeng,<sup>#,○</sup> Nan Yao,<sup>▽</sup> Arun Bansil,<sup>▲</sup> Shuang Jia,<sup>‡,□</sup> Hsin Lin,<sup>§,||</sup> and M. Zahid Hasan<sup>\*,†</sup>

<sup>†</sup>Laboratory for Topological Quantum Matter and Spectroscopy (B7), Department of Physics, Princeton University, Princeton, New Jersey 08544, United States

<sup>‡</sup>International Center for Quantum Materials, School of Physics, Peking University, Peking, China

<sup>§</sup>Centre for Advanced 2D Materials and Graphene Research Centre, National University of Singapore, 6 Science Drive 2, Singapore 117546

<sup>||</sup>Department of Physics, National University of Singapore, 2 Science Drive 3, Singapore 117542

<sup>⊥</sup>Center for Condensed Matter Sciences, National Taiwan University, Taipei 10617, Taiwan

<sup>#</sup>Department of Physics, National Tsing Hua University, Hsinchu 30013, Taiwan

<sup>▽</sup>Princeton Institute for the Science and Technology of Materials, Princeton University, 70 Prospect Avenue, Princeton, New Jersey 08540, United States

<sup>●</sup>Princeton Center for Theoretical Science, Princeton University, Princeton, New Jersey 08544, United States

<sup>○</sup>Institute of Physics, Academia Sinica, Taipei 11529, Taiwan

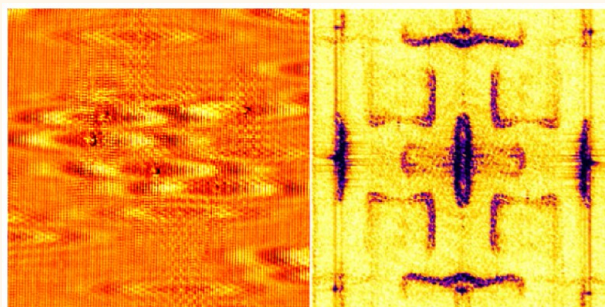
<sup>▲</sup>Department of Physics, Northeastern University, Boston, Massachusetts 02115, United States

<sup>□</sup>Collaborative Innovation Center of Quantum Matter, Beijing, 100871, China

## Supporting Information

**ABSTRACT:** Weyl semimetals may open a new era in condensed matter physics, materials science, and nanotechnology after graphene and topological insulators. We report the first atomic scale view of the surface states of a Weyl semimetal (NbP) using scanning tunneling microscopy/spectroscopy. We observe coherent quantum interference patterns that arise from the scattering of quasiparticles near point defects on the surface. The measurements reveal the surface electronic structure both below and above the chemical potential in both real and reciprocal spaces. Moreover, the interference maps uncover the scattering processes of NbP's exotic surface states. Through comparison between experimental data and theoretical calculations, we further discover that the orbital and/or spin texture of the surface bands may suppress certain scattering channels on NbP. These results provide a comprehensive understanding of electronic properties on Weyl semimetal surfaces.

**KEYWORDS:** Weyl semimetal, topological matter, scanning tunneling microscopy



Understanding and utilization of the surface of topological quantum matter lead to new physics and potential applications.<sup>1–4</sup> A Weyl semimetal is a new topological phase of matter that extends the topological classification beyond insulators, exhibits quantum anomalies, possesses exotic surface Fermi arc electron states, and provides

the first ever realization of Weyl Fermions in physics.<sup>5–11</sup> The surface of a Weyl semimetal has been predicted to exhibit

**Received:** October 28, 2015

**Accepted:** January 8, 2016

**Published:** January 8, 2016



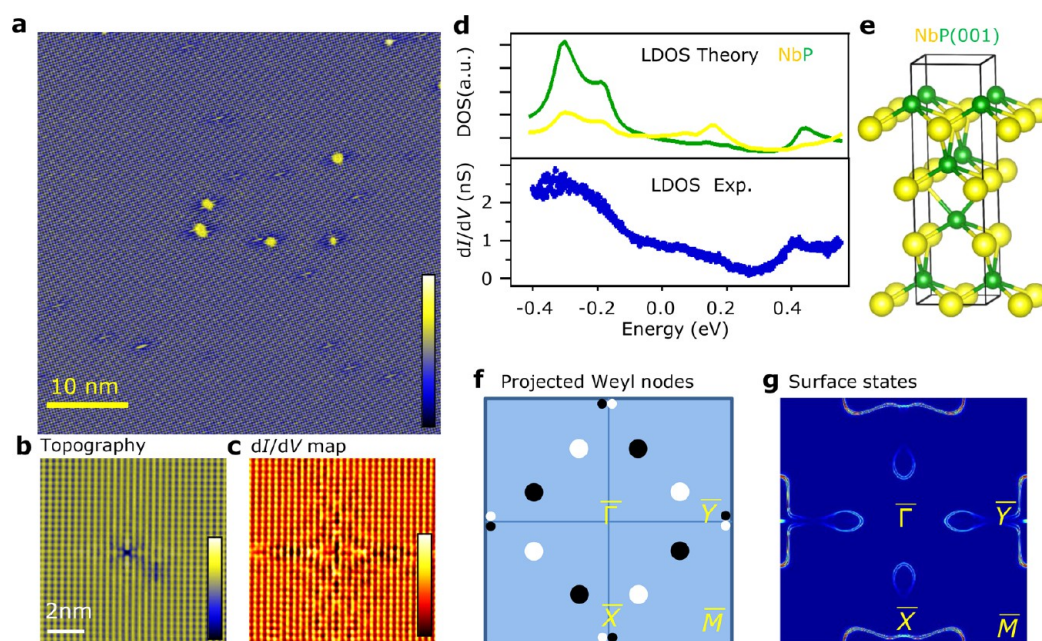


**Figure 1.** Crystalline and electronic properties of the Weyl semimetal NbP(001) surface. (a) Large-scale STM image showing the (001)-surface morphology of the vacuum-cleaved single crystalline NbP. Mapping was performed at 600 mV and 700 pA. On the atomically flat surface, two kinds of typical defects are discerned. Adatoms (or clusters) are shown by yellow spots, and native point defects are shown by white crosses. (b) STM topography and (c)  $dI/dV$  map simultaneously acquired on a point defect (presumably a P vacancy). The measurement setting is  $-120$  mV and 700 pA. (d) Calculated local density of states from the top P (green) and Nb (yellow) atoms on (001)-surfaces of NbP (upper panel) and a measured  $dI/dV$  spectrum (lower panel). The set point of the  $dI/dV$  is 550 mV and 900pA. Direct comparison of the curves confirms our sample was cleaved at (001)-P surface. (e) Schematic of a NbP crystal structure. Nb and P atoms are depicted as yellow and green balls, respectively. (f) Sketch showing the positions of the projected bulk Weyl nodes in the first surface Brillouin zone (not to scale). Large dots represent the well-separated  $W_2$  Weyl nodes, whereas the small dots are the  $W_1$  nodes which are close to each other. Colors stand for the topological charge polarities. (g) Calculated Fermi surface of NbP(001) surface in momentum space. The prominent feature are the two semibowtie-shaped contours at  $\bar{X}$  points, two semiellipses at  $\bar{Y}$  points, and four tadpole-shaped pockets close to at  $\bar{\Gamma}$  points.

interesting tunneling and transport properties due to the existence of exotic bulk Weyl Fermions and Fermi-arc surface states.<sup>12–14</sup> However, for a long period of time, experimental work has been held back owing to the lack of material realization. The very recent discovery of the Weyl semimetal state in the TaAs class of inversion breaking materials, including TaAs, TaP, NbAs, and NbP, has received worldwide attention.<sup>15–22</sup> So far, the surface states of Weyl semimetals have only been accessed by photoemission experiments. Past research on high  $T_c$  superconductors, graphene, and topological materials have established scanning tunneling microscopy (STM) as a powerful tool in understanding the electronic properties of quantum materials with simultaneous spatial, energy, and momentum resolution.<sup>23–30</sup> However, an STM study on a Weyl semimetal's surface remains lacking.

In this article, we present the first atomic-scale visualization of a Weyl semimetal surface *via* scanning tunneling microscopy/spectroscopy. Our measurements show that scatterings by point defects induce quantum interferences on the surface of a Weyl semimetal NbP. Such quantum interference data demonstrate a powerful way to map the surface band structure both below and above the Fermi energy simultaneously in real and reciprocal spaces, both of which are beyond the current photoemission measurements. Furthermore, we identify the different scattering channels on the Weyl semimetal NbP surface and discovered some of them are suppressed due to their orbital and/or spin texture, which is explored here for the first time.

## RESULTS

Figure 1a demonstrates a typical surface morphology of our high quality NbP sample, revealing a large, flat surface ( $50 \times 50$  nm<sup>2</sup>) with very few impurities and defects. The close-up STM image in Figure 1b shows the atomically ordered lattice with only one native point defect on the top atomic layer in the middle of a  $10 \times 10$  nm<sup>2</sup> region. The STM topography indicates a square lattice with a lattice constant  $3.4$  Å which is consistent with the lattice constant  $a = 3.3$  Å determined by the X-ray diffraction.<sup>31,32</sup> This proves that the cleaving plane is the (001) surface. Moreover, the point defect manifests itself as a missing atom in the occupied states (Figure 1b) but a cross-shape bright feature in the empty states (Figure 1a). We speculate that it is a phosphorus (P) vacancy on the surface. The simultaneously obtained differential conductance ( $dI/dV$ ) map in Figure 1c shows the local density of states (LDOS) near the single point defect identified in the topography image. The presence of the defect induces a clear modulation of the LDOS in real space, leading to a four-leaf clover shaped pattern. Similar to the clover-like pattern on the Bi<sub>2</sub>Se<sub>3</sub> surface,<sup>33</sup> the feature in Figure 1c presents a fingerprint of the Weyl semimetal NbP(001) surface. Additionally, we also observe another type of defect, which appears as yellow spots and has a size larger than the point defect (Figure 1a). These are likely to be adatoms or impurity clusters. We take a spectroscopic measurement on a defect-free region (Figure 1d). It shows a finite LDOS at the Fermi level, consistent with the existence of metallic surface states. As displayed in the upper panel of Figure



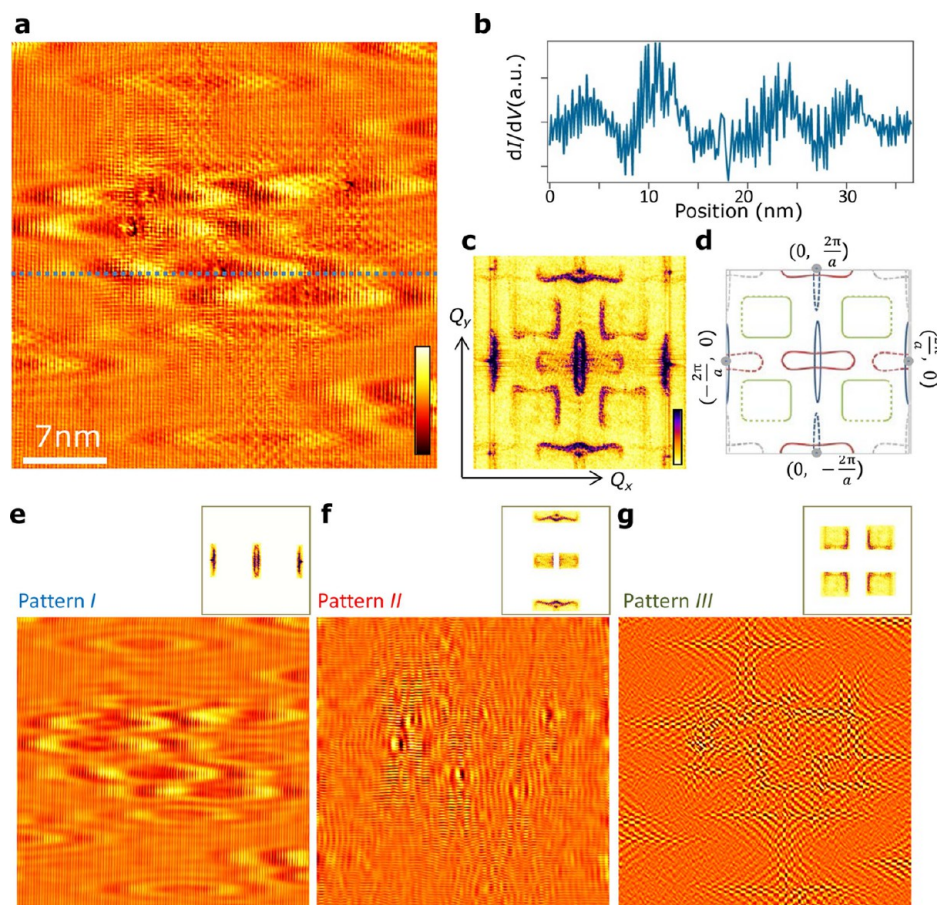


**Figure 2.** Correspondence of real-space modulation to reciprocal-space interference patterns. (a) High-resolution  $dI/dV$  map (80 mV, 700 pA) clearly showing standing-wave modulation patterns induced by quasiparticle interference. The image is of size  $37 \times 37 \text{ nm}^2$  and on a grid of  $256 \times 256$  points. (b) A  $dI/dV$  profile measured along the dotted line in panel a. A long-range standing wave (wavelength about 10 nm) superimposes with corrugations at the atomic level. (c) The fast Fourier transform (FT) of panel a. (d) A sketch of the main features in FT. Resolved in the reciprocal space are three groups of interference patterns which are depicted by different colors. *I*, ellipses (blue) appearing in the center and two Bragg points:  $(2\pi/a, 0)$  and  $(-2\pi/a, 0)$ . *II*, bow-tie-shaped pockets (red) located at  $(0, 0)$  and  $(0, \pm 2\pi/a)$  (another two Bragg points), which are perpendicular to the ellipses. *III*, four rectangles (green) with rounded corners distributed around the centers of each quadrant. Features induced by inter-Brillouin Zone (BZ) scattering are plotted in dotted lines. They are weaker in the data compared to the pockets from intra-BZ scattering. (e–g) Real-space interference patterns corresponding to different FT pockets shown in the upper panels. Fourier filtering allows us to clearly visualize the prominent long-range waves (e) and atomic-scale waves (g), separately.

1d, the calculated LDOS from niobium (Nb) or P atoms in the topmost layer of NbP(001) have different shapes. The measured LDOS ( $dI/dV$ ) is in agreement with calculations for P termination, which indicates that the naturally cleaved NbP(001) surface is terminated by a P atom layer as schematically shown in the structure model in Figure 1e.

We present some essential results of the bulk and surface electronic structure of NbP which can help understand our STM measurements. There are 24 Weyl nodes in the first bulk Brillouin zone (BZ). On the (001) surface, they project as 16 projected Weyl nodes (Figure 1f). We name the 8 projected nodes near the  $\bar{X}$  ( $\bar{Y}$ ) point as  $W_1$  (the small dots in Figure 1f). They have projected chiral charge of  $\pm 1$ . We name the other 8 nodes near the midpoint of the  $\bar{\Gamma} - \bar{X}$  ( $\bar{Y}$ ) lines, with projected chiral charges of  $\pm 2$  as  $W_2$  (the large dots in Figure 1f). Figure 1g shows a calculated Fermi surface of the NbP (001) surface states in momentum space, which is consistent with angle-resolved photoemission electron spectroscopy (ARPES) data.<sup>21,22</sup> We find three dominant features: a tadpole-shaped feature that runs from each midpoint of the  $\bar{\Gamma} - \bar{X}$  ( $\bar{Y}$ ) line toward the  $\bar{X}$  ( $\bar{Y}$ ) point, two semibowtie-shaped pockets at each

$\bar{X}$  point and two semielliptical pockets at each  $\bar{Y}$  point. We note that the number of Fermi arcs terminating on a projected Weyl node must equal the absolute value of its projected chiral charge. Thus, each projected  $W_2$  ( $W_1$ ) node is associated with two (one) Fermi arcs. The head of the tadpole feature is the double Fermi arc associated with each  $W_2$  Weyl node (Supporting Information, Figure S1a,c). The single Fermi arc associated with the  $W_1$  Weyl node is a very short direct line connecting the nearby pair of nodes, and they are too small to be experimentally resolved (Figure S1b,d). Importantly, our calculation also reveals the orbital texture of the NbP (001) surface states. The Fermi contours can be decomposed into different states, which originate from the three  $p$ -orbitals of the P atoms and five  $d$ -orbitals of the Nb atoms. Since the NbP(001) surface is terminated by P atoms, the  $p$ -orbitals of the P atoms dominate in the surface electronic structure. Therefore, we restrict our discussion to the  $p$ -orbital derived surface states. The two tadpole-shaped contours near the midpoint of the  $\bar{\Gamma} - \bar{X}$  ( $\bar{Y}$ ) line have  $p_y$  ( $p_x$ ) character, while the pockets at the zone boundary are mainly derived from the  $p_z$  orbital (Figure S2).

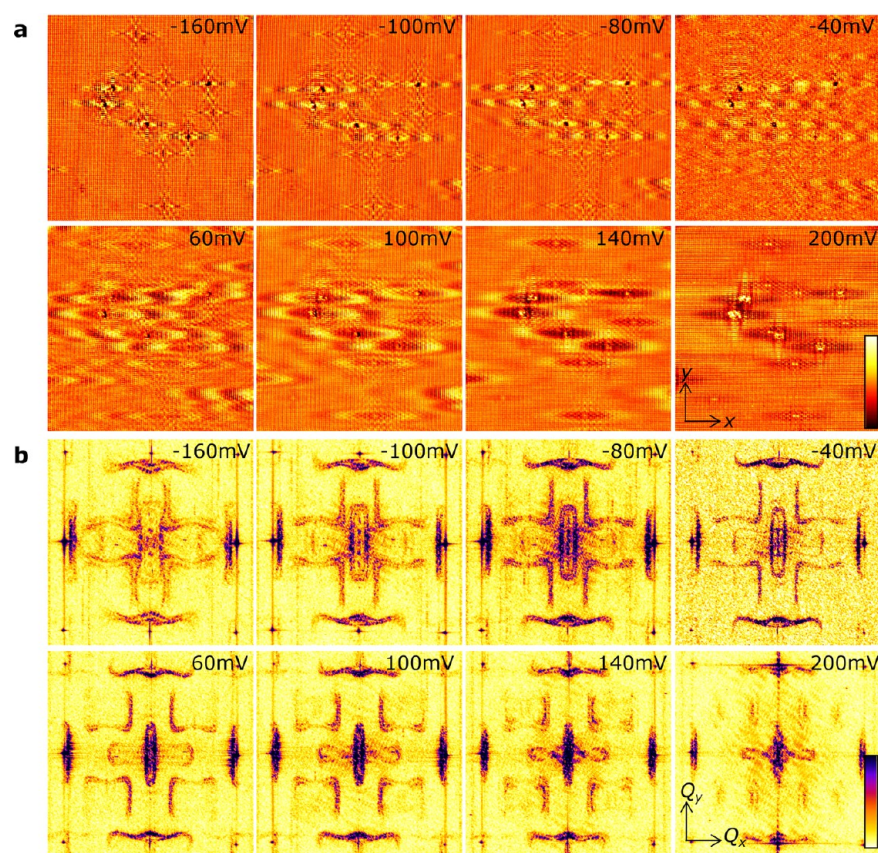


**Figure 3.** Energy-dependent quantum interference patterns from surface quasi-particles of NbP. (a) A series of  $dI/dV$  maps measured at indicated voltages with tunneling current at 700pA (or 500pA when  $V = -40$  mV and 60 mV). All images are of size  $37 \times 37$  nm<sup>2</sup> and on a grid of  $256 \times 256$  points. The two-dimensional electron gas on the NbP surface is scattered by the defects and forms anisotropic standing waves (interference patterns in real space). The pattern shows a  $C_2$  rather than  $C_4$  symmetry. The wavelengths increase with elevated voltages, indicative of hole-like surface quasi-particles. The defects are shown as dark (bright) spots on the maps taken with negative (positive) voltages. (b) Corresponding Fourier transform of each map in panel a. The voltage-dependent evolution of interference patterns (in momentum space) establishes a picture of the exotic surface states in this energy range. At  $-160$  mV, three patterns (ellipses, bowties, and rectangles) are enlarged and merge into each other. Between  $-100$  mV and  $140$  mV, all interference pockets are clearly resolved. Ellipses and rectangles fade away at  $200$  meV while the bowtie pockets remain visible.

Fourier-transform (FT)  $dI/dV$  techniques provide a powerful way to simultaneously study the occupied and unoccupied states of the electronic structure in real and reciprocal (momentum) space.<sup>34</sup> This is not possible by ARPES because photoemission can only probe the occupied states of the electronic structure and lacks spatial resolution. The key is to take advantage of elastic scattering of point defects. On an ideal surface, without any disorder or defects, electronic quasiparticles are Bloch eigenstates characterized by wavevector  $\vec{k}$  and energy  $\epsilon$ . The surface disorder consisting of impurities or crystal defects causes elastic scattering, which mixes eigenstates of different  $\vec{k}$  at the same  $\epsilon(\vec{k})$ . In other words, the presence of a point defect can mix any two states with different momenta  $\vec{k}_1$  and  $\vec{k}_2$  on a constant energy contour, if these two states are coupled by a large matrix element. The mixing of eigenstates with different  $\vec{k}$  leads to quantum interference patterns in the vicinity of the defect, which can be uniquely observed in a  $dI/dV$  map because it measures the LDOS in a spatially resolved fashion. In addition, by Fourier transforming the real space interference patterns, one can gain insight into the electronic structure in momentum space. Furthermore, scattering matrix elements depend on orbital and spin components of the states at different  $\vec{k}$ , therefore the quantum interference can also

reveal orbital and/or spin characters of the electronic states.<sup>25–29</sup>

The  $dI/dV$  map can measure the quasiparticle interference (QPI) patterns in real space while the FT- $dI/dV$  map provides the same QPI information but in reciprocal space, which enables us to study surface electronic structure of NbP(001) in both real and reciprocal spaces. Figure 2a shows a  $dI/dV$  map on a  $37 \times 37$  nm<sup>2</sup> terrace at a bias voltage of 80 mV. Remarkably, we observe clear standing waves as a spatial modulation of the LDOS around a defect on the surface. These “ripples” are related to quantum interference effects that arise from scattering of electron Bloch waves in the presence of crystal defects. The spatial oscillation is clearly seen in the  $dI/dV$  line-cut shown in Figure 2b. We perform a FT on these  $dI/dV$  maps to gain insight into the electronic structure in momentum space (Figure 2c). The elastic scattering that relates two states with  $\vec{k}_1$  and  $\vec{k}_2$ , leads to the interference pattern in the reciprocal space at  $\vec{Q} = (\vec{k}_1 - \vec{k}_2)$ . We now show the FT- $dI/dV$  map in the reciprocal  $Q_x - Q_y$  space (Figure 2c) and divide the dominant features into three groups (Figure 2d), according to their distinct line shapes in  $Q$ -space. (I) We see an elliptical contour centered at the origin of the map,  $[(Q_x, Q_y) = (0, 0)]$ . The long axis is along the  $Q_y$  direction. This feature is repeated at Bragg points  $(Q_x, Q_y) = (\pm 2\pi/a, 0)$  and  $(Q_x, Q_y) = (0, \pm 2\pi/a)$ .



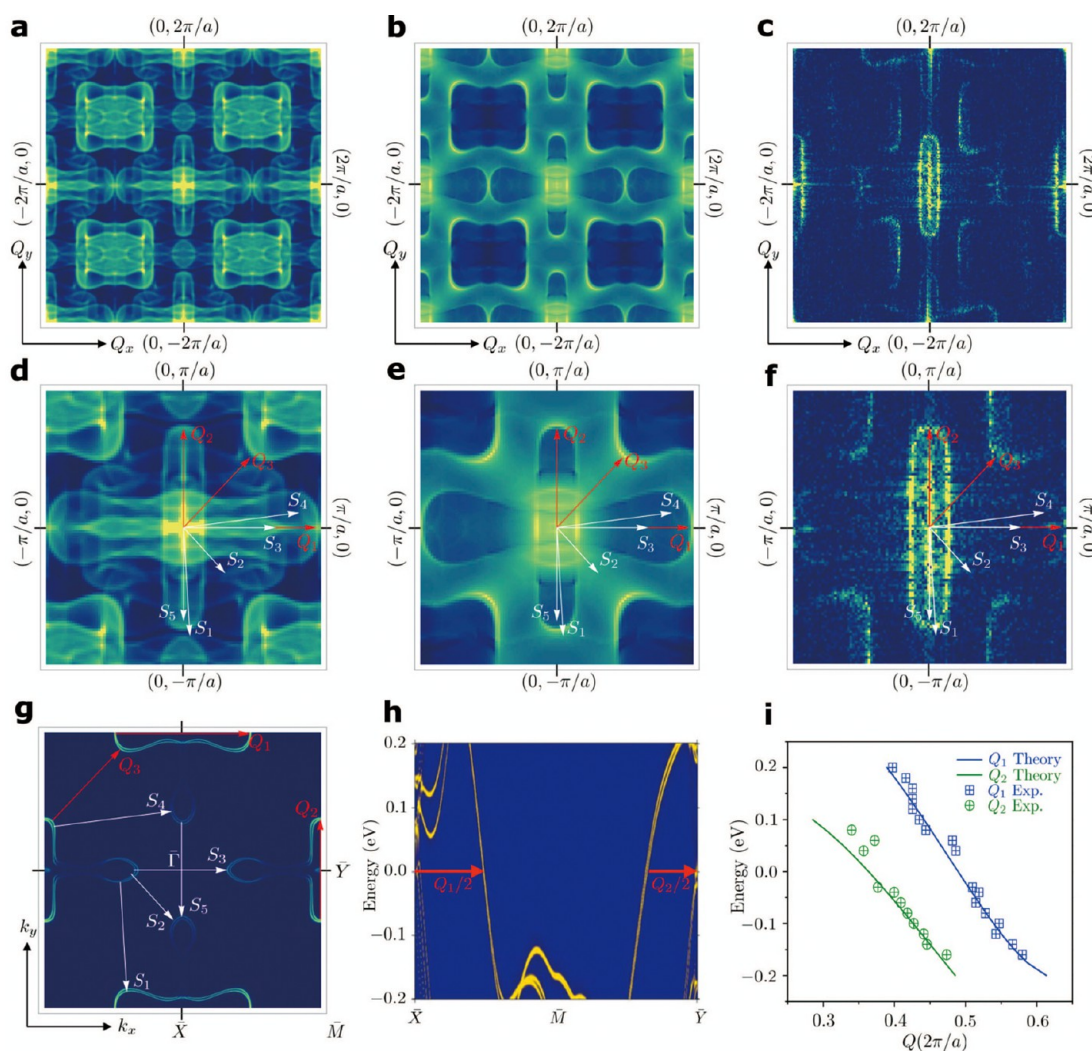


**Figure 4.** QPI pattern arising from scattering between different Fermi pockets. (a) Calculated joint density of states from the Fermi surface of NbP(001) surface. (b) Same as a but with matrix-element effect considered. (c) Fourier transformed dI/dV map measured close to Fermi level ( $-10$  mV). Bragg points are marked with their coordinates in  $Q$ -space. (d–f) Same as panels a–c but with a smaller  $\bar{Q}$  space range of  $Q_x$  ( $Q_y$ )  $\in [-\pi, \pi]$ . (g) Calculated Fermi surface of NbP (001) with intra- and inter-pocket scatterings indicated by white arrows.  $Q_1$  ( $Q_2$ ) stands for inter-pocket scattering within the pocket surrounding  $\bar{X}$  ( $\bar{Y}$ ) while  $Q_3$  is the inter-pocket scattering between the bowtie-shaped and ellipse-shaped Fermi pockets. The white dotted arrows  $S_1$ – $S_3$  represent scattering processes involving the tadpole pockets. (h) Calculated surface band structure of NbP along  $\bar{X} - \bar{M} - \bar{Y}$ . (i) The dispersions of  $Q_1$  (blue) and  $Q_2$  (green) scattering vectors with respect to the bias voltage (energy), indicative of a hole pocket as energy increases. Experimental results (markers) are in good agreement with the theoretical calculations (solid lines).

a). However, we observe that the ones at  $(Q_x, Q_y) = (0, \pm 2\pi/a)$  (noted by the red dotted lines in Figure 2d) have weaker intensities and are barely visible in Figure 2c. (II) Similarly, we find a bowtie-shaped contour centered at the origin and repeated at Bragg points, whose long axis is along the  $Q_x$  direction. The bowtie contours at  $(Q_x, Q_y) = (\pm 2\pi/a, 0)$  are much dimmer and are marked as blue dotted lines in Figure 2d. In addition, we observe weak features at the corners of the map, which suggest that both the elliptical and bowtie-shaped contours are also repeated at the corners,  $(Q_x, Q_y) = (\pm 2\pi/a, \pm 2\pi/a)$ , indicated by the gray dotted line. (III) We observe four contours located within each quadrant of the map. The contours have an approximately rectangular shape. In fact, the vertical edges are nearly straight, whereas the horizontal ones are curvy. For each contour, the two edges that are further away from the origin (noted by the green dotted lines) are obviously

less visible than the two that are closer to the origin (the solid green lines).

We investigate in turn the contribution of each feature in the real space QPI pattern. To do so, we isolate one of the features in the FT-dI/dV map (insets of Figure 2 panels e–g) and perform an inverse FT. This frequency-selected Fourier filtering allows us to visualize the real space interferences that arise from a particular contour in the reciprocal  $Q$ -space. As shown in Figure 2e, the elliptical contour leads to the dominant long-range standing waves. By contrast, the rectangular contours in Figure 2g generate an intricate checkerboard knit, where the wavelength of the ripples/interferences is much shorter (atomic scale). We note that by plainly resolving both long wavelength and atomic corrugations in real space, one obtains a rich quantum interference pattern in momentum space. Furthermore, all of the interference patterns in Figures 2e–g can be

identified back in the raw data, real space  $dI/dV$  map in Figure 2.

Next, we investigate the QPI patterns as a function of energy. Figure 3a shows the real space  $dI/dV$  maps at different bias voltages. Clear quantum interference is seen at all energies. At a bias voltage of  $-160$  mV, which corresponds to the occupied states at a binding energy of  $160$  meV below the Fermi level, we observe that the interference pattern has quite short wavelengths and mainly exists in the close vicinity of the defects. The pattern near each defect is nearly  $C_4$  symmetric. As one increases the bias voltage, we observe that the ripples propagate further away from the defects. It is important to observe the smooth evolution of the wavelength as a function of the bias voltage as in Figure 3a, because this shows that our  $dI/dV$  map is indeed resolving the standing waves of two-dimensional surface quasiparticles, rather than simply imaging the wave functions of the defects.<sup>35</sup> In the energy range  $-100$  mV to  $+140$  mV, the dominant wavelength becomes larger with more positive bias voltage (a larger wavelength in real space corresponds to a smaller wavevector  $\vec{Q}$  in reciprocal space), and the pattern becomes increasingly  $C_4$  breaking. At high bias voltages for mapping the unoccupied states of the electronic structure, such as  $+200$  mV, the dominant interference discussed above is not observed because its wavelength becomes comparable to the size of the image. Some other weak interference with shorter wavelengths is still observable. We emphasize that the clear visualization of surface standing waves (the several sets of wave peaks and valleys explicitly resolved) has not been routinely obtained on other topological materials, and is not a trivial result as well. Combining with the atomic manipulation capability of STM, one can derive quantum phase information on the surface quasiparticle wave function.<sup>36</sup> This may open the possibility to extract topological information contained in the Berry phase of the Weyl Fermions.

The observed features in real space have a nice correspondence to the FTs in  $Q$ -space, shown in Figure 3b. Specifically, the FT- $dI/dV$  map at  $-200$  mV is approximately  $C_4$  symmetric. However, at more positive bias voltages, for example, the one at  $-40$  mV, the FT- $dI/dV$  maps clearly break  $C_4$  symmetry. The  $C_4$  breaking surface state electronic structure of NbP can be understood by considering its crystal structure, where the rotational symmetry is implemented as a screw axis that sends the crystal back into itself after a  $C_4$  rotation and a translation by  $c/2$  along the rotation axis. Therefore, even though rotation axis is normal to the (001) surface, it still breaks  $C_4$  symmetry. Furthermore, we observe that the size of the pockets shrinks as one increase the bias voltage, consistent with the increasing wavelength seen in real space. It proves that the surface bands are formed by hole-like quasiparticles.

## DISCUSSIONS

We theoretically compute NbP's QPI patterns. In general, the QPI calculation depends on the spin and orbital matrix element between the initial and final state of a scattering event. The spin-dependence is fully constrained in the case of nonmagnetic impurities: only elastic scattering between states of the same spin is allowed. The orbital matrix element cannot be easily predicted theoretically as it depends on the details of the impurity potential. In Figure 4a,b, we provide two extreme limits, that is, a calculation that allows all elastic scatterings (Figure 4a), which is the joint density of states (JDOS), and the calculation that forbids any scatterings between states of

different orbitals or opposite spins (Figure 4b). Although neither of them may completely capture the reality of our experiment, these calculations provide useful references that help to interpret our data.

Specifically, the features that are prominent in Figure 4a but suppressed in Figure 4b must arise from scattering between states with very different orbital character and/or spin polarization. For example, the square-shaped patterns in each quadrant are filled with intensity in Figure 4a, whereas they are empty in Figure 4b. Moreover, a circular feature around  $\vec{Q} = (0, \pi/a)$  is seen in Figure 4a but it is missing in Figure 4b. By further comparing these calculated QPIs with the surface Fermi surface, we find that this circular feature in Figure 4a can be associated with the scattering between the tadpole and the bow-tie surface states, as indicated by the scattering vector  $S_1$  in Figure 4g. Because the tadpole surface states arise from the  $p_x$  and  $p_y$  orbitals, whereas the bowtie surface states arise from the  $p_z$  orbital, we see that this circular feature in Figure 4a is suppressed in Figure 4b because the corresponding scattering  $S_1$  is between two states of dominantly different orbitals.

We compare these two calculations (Figure 4 panels a and b) with our STM data (Figure 4c). It can be seen clearly that the features that are prominent in Figure 4a but suppressed in Figure 4b are also very weak in the STM data. For example, in the  $Q$  space region that corresponds to the circular feature in Figure 4a, there are only weak residual intensities in our STM data (Figure 4c), which cannot be interpreted as a clear feature. The same case can be made for the  $Q$  region inside each square feature. Through this comparison, we conclude that in our experiment the scattering between states of different orbital character or opposite spin polarization is suppressed.

We further search for features in the QPI that arise from the scatterings involving Fermi arcs. As we have mentioned above, the Fermi arcs associated with the  $W_1$  Weyl nodes are extremely short, and hence we do not expect them to give any significant signal in the QPI. On the other hand, the Fermi arcs associated with the  $W_2$  Weyl nodes are the head of the tadpole surface states. We highlight the scattering vectors  $S_1$ – $S_5$  as those that are associated with Fermi arcs in Figure 4d. We can identify features related to each of these scattering vectors in the JDOS calculation (Figure 4a,d). The scattering vectors  $S_1$ ,  $S_2$ , and  $S_4$  connect two states of dominantly different orbital character. Therefore, they are strongly suppressed in the calculation that forbids scatterings between different orbitals (Figure 4b,e). In contrast,  $S_3$  and  $S_5$  are scattering processes between states of the same orbital character. Therefore, they are still visible in the calculation that includes the matrix element effect (Figure 4b,e), but they are very weak overall because the spectral weight of the tadpole surface states is very low (Figure 4g). In our STM data, we found that the intensity at the  $Q$  regions that correspond to the  $S_1$ – $S_5$  vectors is very weak. Therefore, we conclude that the scatterings that arise from the tadpole surface states are suppressed in our experiment owing to the matrix element effect and the low spectral weight of the tadpole surface states.

We further notice that some of the features in the STM data (Figures 3b and 4c) contain double lines. The most obvious one is the rectangular feature as shown in Figure 3b. We also note that the splitting between the double lines is the smallest near the Fermi level and becomes larger at higher energies. Currently we do not understand their origin. Both calculations (Figures 4a,b) cannot produce such 2-fold features. Since our calculation only considers elastic scattering, we speculate that

the energy dependent double line features may be due to inelastic scattering processes or due to many-body effects.

Next, we consider the scatterings that arise from the prominent surface state contours, namely the scattering vectors  $Q_1$ – $Q_3$  (Figure 4d). The scattering vector  $Q_1$  in  $k$ -space gives rise to the bowtie-shaped feature at the origin  $[(Q_x, Q_y) = (0, 0)]$  of  $Q$ -space. Similarly, the vector  $Q_2$  leads to the elliptical feature at the center of  $Q$ -space. We can also draw a vector which connects two bowtie-shaped contours (or two elliptical contours) located at different  $\bar{X}$  ( $\bar{Y}$ ) points. This scattering process generates the replicas of the bowtie-shaped or elliptical features at the boundaries and the corners in  $Q$ -space. Finally, the scattering vector  $Q_3$  connects a bowtie-shaped contour at a  $\bar{X}$  point to an elliptical contour at a  $\bar{Y}$  point in  $k$ -space. This induces the square-shaped features at every quadrant of  $Q$ -space. The agreement between theory and experiment is quite remarkable considering the rich structure of the Fermi surface and QPI pattern.

Since the QPI data arise from the surface states, we can measure the surface band structure both below and above the Fermi level from our STM data. For example,  $Q_1$  connects the two end points of the bowtie on the high symmetry line,  $\bar{X}$ – $\bar{M}$ , in  $k$ -space. As a result, there is a simple relationship between the scattering vector  $\vec{Q}$  and momentum  $\vec{k}$ , namely  $\vec{k} = \vec{Q}/2$  along the  $\bar{X}$ – $\bar{M}$  direction. This simple relationship allows us to directly obtain the band structure,  $\varepsilon(\vec{k})$  along the  $\bar{X}$ – $\bar{M}$  line (if one neglects the spin splitting of the bands which is indeed small in NbP comparing to TaAs, see more details in Supporting Information Figure S3). The other intrapocket scattering vector  $Q_2$  can give similar information. The experimental data marked in Figure 4f are in agreement with the model calculation (solid lines) derived from the band structure as shown in Figure 4e, which also agrees well with our ARPES measured surface band structure.<sup>22</sup> We therefore can determine the Fermi velocity to be 2.2 eVÅ and 1.6 eVÅ along  $\bar{X}$ – $\bar{M}$  direction and along  $\bar{Y}$ – $\bar{M}$ , respectively.

## CONCLUSION

In summary, we have for the first time visualized the novel surface of a Weyl semimetal with atomic scale spatial resolution. We are able to clearly observe the quantum interferences on a Weyl semimetal's surface and study its QPI pattern. This has enabled us to resolve clear quantum interference patterns simultaneously in real and momentum spaces. The voltage-dependent real-space imaging allows us to clearly resolve the evolution of the surface standing waves. It opens the door to measuring the phase of wave function in topological quantum matter. The main features observed in the QPI pattern arise from the topologically trivial contours. This finding suggests that the scattering is dominated by the trivial surface states, whereas the scatterings that arise from the Fermi arcs are suppressed due to spin and orbital effects. Our QPI results in reciprocal space reveal the orbital and spin matrix element effects that are critical to the scattering processes on the surface. It helps to understand the surface properties of the only available Weyl semimetal class TaAs, TaP, NbAs, and NbP and sheds light on the future research of Weyl semimetals-based nanomaterials and nanodevices.

## METHODS

Single crystalline NbP samples were grown by standard chemical vapor transport methods. The samples were cleaved at 79 K in an ultrahigh-vacuum chamber and were immediately transferred *in vacuo* to a

Unisoku STM operated at 4.6 K and  $\sim 10^{-11}$  mbar. Chemically etched Pt/Ir tips were used. Constant-current mode STM images were obtained by applying a voltage to the sample. A lock-in amplifier was employed to get the first differentiated ( $dI/dV$ ) signal with a modulation at 1 to 8 mV and 1 kHz. The  $dI/dV$  maps were measured with STM images, using the same method as in refs 26 and 27. We processed the STM images and  $dI/dV$  maps in the WsXM software. The FTs were performed directly from the raw data. All color bars in the figures are in linear scale. Surface electronic band structures were obtained by a Wannier function based Hamiltonian in a semi-infinite slab using the recursive Green's function method. The surface Green's functions are used to calculate the interference patterns (see Supporting Information for more details).

## ASSOCIATED CONTENT

### Supporting Information

The Supporting Information is available free of charge on the ACS Publications website at DOI: 10.1021/acsnano.5b06807.

A brief statement of the Fermi arcs of NbP(001) and the calculation methods (PDF)

## AUTHOR INFORMATION

### Corresponding Author

\*E-mail: mzhassan@princeton.edu.

### Author Contributions

H.Z., S.-Y.X., and G.B. contributed equally to this work.

### Notes

The authors declare no competing financial interest.

## ACKNOWLEDGMENTS

The STM measurements at Princeton University were supported by the Gordon and Betty Moore Foundations EPIQS Initiative through Grant GBMF4547 (Hasan). Theoretical calculations at National University of Singapore were supported by the National Research Foundation, Prime Minister's Office, Singapore, under its NRF fellowship (NRF Award No. NRF-NRFF2013-03). NbP crystal growth was supported by National Basic Research Program of China (Grant No. 2013CB921901 and 2014CB239302). F.C. acknowledges the support provided by MOST-Taiwan under Project No. 102-2119-M-002-004. This work was also supported in part by the National Science Foundation-MRSEC program through the Princeton Center for Complex Materials (DMR-1420541; NY, FW). T.-R.C. and H.-T.J. are supported by National Science Council, Academia Sinica, and National Tsing Hua University, Taiwan, and also thank NCHC, CINC-NTU, and NCTS, Taiwan, for technical support. The work at Northeastern University was supported by the US Department of Energy (DOE), Office of Science, Basic Energy Sciences Grant No. DE-FG02-07ER46352, and benefited from Northeastern University's Advanced Scientific Computation Center (ASCC) and the NERSC supercomputing center through DOE Grant No. DE-AC02-05CH11231.

## REFERENCES

- Hasan, M. Z.; Xu, S.-Y.; Neupane, M. Topological Insulators, Topological Dirac Semimetals, Topological Crystalline Insulators, and Topological Kondo Insulators. In *Topological Insulators: Fundamentals and Perspectives*; John Wiley & Sons: 2015.
- Hasan, M. Z.; Xu, S.-Y.; Bian, G. Topological Insulators, Helical Topological Superconductors and Weyl Fermion Semimetals. *Phys. Scr.* **2015**, T164, 014001.
- Qi, X.-L.; Zhang, S.-C. Topological Insulators and Superconductors. *Rev. Mod. Phys.* **2011**, 83, 1057–1110.



- (4) Hasan, M. Z.; Kane, C. L. Topological Insulators. *Rev. Mod. Phys.* **2010**, *82*, 3045–3067.
- (5) Turner, A. N.; Vishwanath, A. Beyond Band Insulators: Topology of Semi-Metals and Interacting Phases. In *Topological Insulators*; Elsevier: 2013.
- (6) Weyl, H. Elektron und Gravitation. *Eur. Phys. J. A* **1929**, *56*, 330–352.
- (7) Nielsen, H. B.; Ninomiya, M. The Adler-Bell-Jackiw Anomaly and Weyl Fermions in a Crystal. *Phys. Lett. B* **1983**, *130*, 389–396.
- (8) Balents, L. Weyl Electrons Kiss. *Physics* **2011**, *4*, 36.
- (9) Wan, X.; Turner, A. M.; Vishwanath, A.; Savrasov, S. Y. Topological Semimetal and Fermi Arc Surface States in the Electronic Structure of Pyrochlore Iridates. *Phys. Rev. B: Condens. Matter Mater. Phys.* **2011**, *83*, 205101.
- (10) Burkov, A. A.; Balents, L. Weyl Semimetal in a Topological Insulator Multilayer. *Phys. Rev. Lett.* **2011**, *107*, 127205.
- (11) Xu, S.-Y.; Liu, C.; Kushwaha, S. K.; Sankar, R.; Krizan, J. W.; Belopolski, I.; Neupane, M.; Bian, G.; Alidoust, N.; Chang, T.-R.; Jeng, H.-T.; Huang, C.-Y.; Tsai, W.-F.; Lin, H.; Shibaev, P. P.; Chou, F.-C.; Cava, R. J.; Hasan, M. Z. Observation of Fermi Arc Surface States in a Topological Metal. *Science* **2015**, *347*, 294–298.
- (12) Ojanen, T. Helical Fermi Arcs and Surface States in Time Reversal Invariant Weyl Semimetals. *Phys. Rev. B: Condens. Matter Mater. Phys.* **2013**, *87*, 245112.
- (13) Hosur, P. Friedel Oscillations due to Fermi Arcs in Weyl Semimetals. *Phys. Rev. B: Condens. Matter Mater. Phys.* **2012**, *86*, 195102.
- (14) Potter, A. C.; Kimchi, I.; Vishwanath, A. Quantum Oscillations from Surface Fermi Arcs in Weyl and Dirac Semimetals. *Nat. Commun.* **2014**, *5*, 5161.
- (15) Huang, S.-M.; Xu, S.-Y.; Belopolski, I.; Lee, C.-C.; Chang, G.; Wang, B.; Alidoust, N.; Bian, G.; Neupane, M.; Zhang, C.; Jia, S.; Bansil, A.; Lin, H.; Hasan, M. Z. A Weyl Fermion Semimetal with Surface Fermi Arcs in the Transition Metal Monopnictide TaAs Class. *Nat. Commun.* **2015**, *6*, 7373.
- (16) Weng, H.; Fang, C.; Fang, Z.; Bernevig, B. A.; Dai, X. Weyl Semimetal Phase in Noncentrosymmetric Transition Metal Monophosphides. *Phys. Rev. X* **2015**, *5*, 011029.
- (17) Xu, S.-Y.; Belopolski, I.; Alidoust, N.; Neupane, M.; Bian, G.; Zhang, C.; Sankar, R.; Chang, G.; Yuan, Z.; Lee, C.-C.; Huang, S.-M.; Zheng, H.; Ma, J.; Sanchez, D. S.; Wang, B.; Bansil, A.; Chou, F.; Shibaev, P. P.; Lin, H.; Jia, S.; et al. Discovery of a Weyl Fermion Semimetal and Topological Fermi Arcs. *Science* **2015**, *349*, 613–617.
- (18) Lv, B. Q.; Weng, H. M.; Fu, B. B.; Wang, X. P.; Miao, H.; Ma, J.; Richard, P.; Huang, X. C.; Zhao, L. X.; Chen, G. F.; Fang, Z.; Dai, X.; Qian, T.; Ding, H. Experimental Discovery of Weyl Semimetal TaAs. *Phys. Rev. X* **2015**, *5*, 031013.
- (19) Xu, S.-Y.; Alidoust, N.; Belopolski, I.; Yuan, Z.; Bian, G.; Chang, T.-R.; Zheng, H.; Strocov, V. N.; Sanchez, D. S.; Chang, G.; Zhang, C.; Mou, D.; Wu, Y.; Huang, L.; Lee, C.-C.; Huang, S.-M.; Wang, B.; Bansil, A.; Jeng, H.-T.; Neupert, T.; et al. Discovery of a Weyl Fermion State with Fermi Arcs in Niobium Arsenide. *Nat. Phys.* **2015**, *11*, 748–754.
- (20) Xu, S.-Y.; Belopolski, I.; Sanchez, D. S.; Guo, C.; Chang, G.; Zhang, G.; Bian, G.; Yuan, Z.; Lu, H.; Feng, Y.; Chang, T.-R.; Shibaev, P. P.; Prokopovych, M. L.; Alidoust, N.; Zheng, H.; Lee, C.-C.; Huang, S.-M.; Sankar, R.; Chou, F.; Hsu, C.-H.; et al. Experimental Discovery of a Topological Weyl Semimetal State in TaP. *Sci. Adv.* **2015**, *1*, e1501094.
- (21) Xu, D. F.; Du, Y.-P.; Wang, Z.; Li, Y.-P.; Niu, X.-H.; Yao, Q.; Pavel, D.; Xu, Z.-A.; Wan, X.-G.; Feng, D.-L. Observation of Fermi Arcs in Nnon-Centrosymmetric Weyl Semi-metal Candidate NbP. *Chin. Phys. Lett.* **2015**, *32*, 107101.
- (22) Belopolski, I.; Xu, S.-Y.; Sanchez, D. S.; Chang, G.; Guo, C.; Neupane, M.; Zheng, H.; Lee, C.-C.; Huang, S.-M.; Bian, G.; Alidoust, N.; Chang, T.-R.; Wang, B.; Zhang, X.; Bansil, A.; Jeng, H.-T.; Lin, H.; Jia, S.; Hasan, M. Z. Observation of Surface States Derived from Topological Fermi Arcs in the Weyl Semimetal NbP. *Cond. Mater.* **2015**, arxiv: 1509.07465.
- (23) Rutter, R. M.; Crain, J. N.; Guisinger, N. P.; Li, T.; First, P. N.; Strosio, J. A. Scattering and Interference in Epitaxial Graphene. *Science* **2007**, *317*, 219–222.
- (24) Fujita, K.; Hamidian, M.; Firmo, I.; Mukhopadhyay, S.; Kim, C. K.; Eisaki, H.; Uchida, S.; Davis, J. C. Spectroscopic Imaging STM: Atomic-Scale Visualization of Electronic Structure and Symmetry in Underdoped Cuprates. In *Strongly Correlated Systems-Experimental Techniques*; Springer: 2014.
- (25) Roushan, P.; Seo, J.; Parker, C. V.; Hor, Y. S.; Hsieh, D.; Qian, D.; Richardella, A.; Hasan, M. Z.; Cava, R. J.; Yazdani, A. Topological Surface States Protected from Backscattering by Chiral Spin Texture. *Nature* **2009**, *460*, 1106–1109.
- (26) Zhang, T.; Cheng, P.; Chen, X.; Jia, J.-F.; Ma, X.; He, K.; Wang, L.; Zhang, H.; Dai, X.; Fang, Z.; Xie, X.; Xue, Q.-K. Experimental Demonstration of Topological Surfaces Protected by Time-Reversal Symmetry. *Phys. Rev. Lett.* **2009**, *103*, 266803.
- (27) Sessi, P.; Reis, F.; Bathon, T.; Kokh, K. A.; Tereshchenko, O. E.; Bode, M. Signatures of Dirac Fermion-Mediated Magnetic Order. *Nat. Commun.* **2014**, *5*, 5349.
- (28) Lee, I.; Kim, C. K.; Lee, J.; Billinge, S. J. L.; Zhong, R.; Schneeloch, J. A.; Liu, T.; Valla, T.; Tranquada, J. M.; Gu, G.; Davis, J. C. S. Imaging Dirac-Mass Disorder from Magnetic Dopant Atoms in the Ferromagnetic Topological Insulator  $\text{Cr}_x(\text{Bi}_{0.1}\text{Sb}_{0.9})_{2-x}\text{Te}_3$ . *Proc. Natl. Acad. Sci. U. S. A.* **2015**, *112*, 1316–1321.
- (29) Zeljkovic, I.; Okada, Y.; Huang, C.-Y.; Sankar, R.; Walkup, D.; Zhou, W.; Serbyn, M.; Chou, F.; Tsai, W.-F.; Lin, H.; Bansil, A.; Fu, L.; Hasan, M. Z.; Madhavan, V. Mapping the Unconventional Orbital Texture in Topological Crystalline Insulators. *Nat. Phys.* **2014**, *10*, 572–577.
- (30) Jeon, S.; Zhou, B. B.; Gyenis, A.; Feldman, B. E.; Kimchi, I.; Potter, A. C.; Gibson, Q. D.; Cava, R. J.; Vishwanath, A.; Yazdani, A. Landau Quantization and Quasiparticle Interference in the Three-Dimensional Dirac Semimetal  $\text{Cd}_3\text{As}_2$ . *Nat. Mater.* **2014**, *13*, 851–856.
- (31) Murray, J. J.; Taylor, J. B.; Calvert, L. D.; Wang, Y.; Gabe, E. J.; Despault, J. G. Phase Relationships and Thermodynamics of Refractory Metal Pnictides: The Metal-Rich Tantalum Arsenides. *J. Less-Common Met.* **1976**, *46*, 311–320.
- (32) Xu, J.; Greenblatt, M.; Emge, T.; Hoehn, P.; Hughbanks, T.; Tian, Y. Crystal Structure, Electrical Transport, and Magnetic Properties of Niobium Monophosphide. *Inorg. Chem.* **1996**, *35*, 845–849.
- (33) Kim, S.; Ye, M.; Kuroda, K.; Yamada, Y.; Krasovskii, E. E.; Chulkov, E. V.; Miyamoto, K.; Nakatake, M.; Okuda, T.; Ueda, Y.; Shimada, K.; Namatame, H.; Taniguchi, M.; Kimura, A. Surface Scattering via Bulk Continuum States in the 3D Topological Insulator  $\text{Bi}_2\text{Se}_3$ . *Phys. Rev. Lett.* **2011**, *107*, 056803.
- (34) Hoffman, J. E.; McElroy, K.; Lee, D.-H.; Lang, K. M.; Eisaki, H.; Uchida, S.; Davis, J. C. Imaging Quasiparticle Interference in  $\text{Bi}_2\text{Sr}_2\text{CaCu}_2\text{O}_{8+\delta}$ . *Science* **2002**, *297*, 1148–1151.
- (35) Ebert, Ph. Nano-Scale Properties of Defects in Compound Semiconductor Surfaces. *Surf. Sci. Rep.* **1999**, *33*, 121–303.
- (36) Moon, C. R.; Mattos, L. S.; Foster, B. K.; Zeltzer, G.; Ko, W.; Manoharan, H. C. Quantum Phase Extraction in Isospectral Electronic Nanostructures. *Science* **2008**, *319*, 782–787.